This is a preprint, the final version is subject to change, of the American Mineralogist (MSA)
Cite as Authors (Year) Title. American Mineralogist, in press.
DOI: https://doi.org/10.2138/am-2020-7118

Revision 1

Cassiterite crystallization experiments in alkali carbonate aqueous solutions using a hydrothermal diamond-anvil cell

YONGCHAO LIU[1], JIANKANG LI[1,*], AND I-MING CHOU[2]

[1]MNR Key Laboratory of Metallogeny and Mineral Assessment, Institute of Mineral Resources, Chinese Academy of Geological Sciences, Beijing 100037, China

[2]CAS Key Laboratory for Experimental Study under Deep-sea Extreme Conditions, Institute of Deep-sea Science and Engineering, Chinese Academy of Sciences, Sanya, Hainan 572000, China

[*]Corresponding author: Li9968@126.com

Abstract

Ore-forming fluids enriched in alkali carbonate are commonly observed in natural melt and fluid inclusions associated with tin mineralization, particularly in granitic pegmatite. However, the roles of alkali carbonates remain unclear. Hence, to investigate the roles of alkali carbonate, herein, cassiterite (SnO_2) crystallization experiments in SnO_2–Li_2CO_3–H_2O and SnO_2–Na_2CO_3–H_2O systems were conducted using a hydrothermal diamond-anvil cell. The results showed that SnO_2 could dissolve into the alkali carbonate aqueous solution during heating, and long prismatic cassiterite crystals grew during the subsequent cooling stage at average rates of 0.61×10^{-6}–8.22×10^{-6} cm/s in length and 3.40–19.07 $\mu m^3/s$ in volume. The mole fraction of cassiterite crystallized from the SnO_2–Li_2CO_3–H_2O system ranges from 0.03 to 0.41 mol%, which depends on the Li_2CO_3 content dissolved in the aqueous solution. In situ Raman analysis of the alkali carbonate-rich aqueous solution in the sample chamber suggests that the dissolution of SnO_2 can be attributed to the alkaline conditions produced by hydrolysis of alkali carbonate, in which $Sn(OH)_6^{2-}$ may be a potential tin-transporting species. The

cassiterite crystallization conditions obtained in our SnO_2–alkali carbonate–H_2O systems primarily fell within the 400–850 °C and 300–850 MPa temperature and pressure ranges, respectively; further, cassiterite crystallization ended in rare metal pegmatite-forming conditions. These crystallization features of cassiterite are similar to those formed in tin-mineralized granitic pegmatites. It indicates that an alkali carbonate-rich aqueous solution or hydrous melt can work as a favorable transport medium for tin and provides the necessary conditions for cassiterite crystallization in granitic pegmatite, bearing the roles in decreasing the viscosity of hydrous melts and enhancing the solubility of SnO_2 in ore-forming melts or fluids. These roles of alkali carbonate can also be extended for the mineralization of other rare metals (e.g., Li and Be) in granitic pegmatite.

Keywords: Cassiterite, alkali carbonate, pegmatite, crystallization, hydrothermal diamond-anvil cell

INTRODUCTION

Cassiterite (SnO_2) is a predominant tin ore mineral (Kamilli et al. 2017); however, the physicochemical parameters for its formation remain debatable (Audétat et al. 1998; Linnen 1998; Naumov et al. 2011; Korges et al. 2018). Thermodynamic calculations have indicated the presence of tin as hydroxide complexes in water (Jackson and Helgeson 1985), and it is well known that the solubility of cassiterite is highly temperature-dependent (Štemprok 1990; Wilson and Eugster 1990; Bhalla et al. 2005). The tin deposit formation process has been linked to the mobility of tin as Sn(II)–Cl or F complexes in reduced acid fluids, while the precipitation of tin as cassiterite requiring oxidation and acid liberation (Li 1989; Heinrich 1990; Taylor and Wall 1993; Linnen et al. 1995; Sherman et al. 2000; Müller and Seward 2001; Duc-Tin et al. 2007).

However, Schmidt (2018) demonstrated that tin can be transported in the form of Sn(IV)–Cl complexes, such that HCl molality is a crucial parameter for cassiterite precipitation, and pH, pressure, and temperature are less important parameters.

In addition, there is increasing evidence that the capability of CO_2/carbonate-rich fluids to transport some metals at high temperatures and pressures can be significant (Phillips and Evans 2004; Jones et al. 2013; Kokh et al. 2017; Li et al. 2018). The mineral-forming fluids in many tin deposits, especially in tin-mineralized granitic pegmatite, bear low salinity and high alkali carbonate (e.g., Li_2CO_3, Na_2CO_3, Cs_2CO_3, K_2CO_3) concentrations, but only trace quantities of the typical pegmatite-forming fluxes (e.g., F, Cl) (Fu et al. 1993; Fu and Kwak 1994; Rickers et al. 2006; Thomas and Davidson 2016). For example, cassiterite hosts carbonate/bicarbonate-rich melt inclusions in the Ehrenfriedersdorf pegmatite, Germany (Thomas et al. 2006a). These features suggest that alkali carbonates may play important roles in tin mineralization (Kosals 1976; Thomas et al. 2011). Furthermore, alkali carbonate-rich fluids are not rare in granite pegmatites. Carbonate-rich melt and fluid inclusions are found in quartz, feldspar, spodumene, and beryl of many pegmatites (e.g., Bikita in Zimbabwe, Tanco in Canada, Erzgebirge and Zinnwald in Germany, Jiajika and Zhawulong in China) (Anderson et al. 2001; Thomas et al. 2006b, 2012; Li et al. 2017; Xiong et al. 2019). The carbonate content in fluid inclusions is 35.0% (g/g) $NaHCO_3$ in Orlovka pegmatite, Transbaikalia, Russia and 40.0% (g/g) $KHCO_3$ in Nb–Ta-pegmatites from the northern part of Mozambique (Thomas et al. 2011). However, the roles of alkali carbonates have rarely been investigated. Here, following the method of crystallization experiment using a hydrothermal diamond-anvil cell (HDAC) (Li et al. 2013, 2018), cassiterite crystallization experiments in alkali carbonate-rich fluids were conducted to further investigate the roles of alkali carbonates in tin mineralization.

This is a preprint, the final version is subject to change, of the American Mineralogist (MSA)
Cite as Authors (Year) Title. American Mineralogist, in press.
DOI: https://doi.org/10.2138/am-2020-7118

EXPERIMENTAL METHODS

To explore the roles of alkali carbonate in cassiterite formation through in situ monitoring and measurement experiments, the starting materials prepared for the experiments were SnO_2 sintered lump (99.9% purity, Alfa Aesar), Li_2CO_3 powder (≥99.0% purity, Alfa Aesar), and Na_2CO_3 powder (≥99.5% purity, Alfa Aesar).

All experiments were conducted in an improved Bassett-type HDAC (HDAC-VT type, Bassett et al. 1993, 1996; Chou 2003; Li et al. 2016). The sample chamber consisted of a hole (0.5-mm diameter) at the center of a rhenium gasket (3.0-mm diameter, 0.25-mm thickness) that was sealed by compressing two parallel diamond-anvil culets. The sample chamber was heated via external resistive heating using two tungsten carbide seats, each of which was wrapped with a Mo heating resistance wire. The temperature in the sample chamber was measured using two K-type thermocouples, whose junctions were attached to the diamonds near the sample chamber. The thermocouples were calibrated via repeated measurements of the melting points of $NaNO_3$ (306.8 °C) and NaCl (800.5 °C). The accuracy of the reported temperature was ±1 °C. An Olympus BX51TRF microscope was used to directly observe the sample, and images of the entire sample chamber were continuously recorded during the experiments via a digital camera.

Considering the thermal expansion of a rhenium gasket during heating, the pretreatment of a new rhenium gasket was conducted to ensure that the sample chamber was approximately isochoric during the crystallization experiments (Chou 1996). During the pretreatment, the sample chamber, which was loaded with pure water and a vapor bubble, was heated to 850 °C and then cooled to ambient temperature at 20 °C/min in several repeated cycles until the vapor

bubble-disappearing temperature, measured for the vapor bubble generated during the cooling process, was less than 1 °C below that measured during the previous heating process.

For the SnO_2–Li_2CO_3–H_2O experiments, a sintered SnO_2 lump, Li_2CO_3 powder, and distilled water were loaded into the HDAC sample chamber at room temperature (24 °C) (Fig. 1a). The sample chamber was first heated at a rate of 5 °C/min until the Li_2CO_3 and SnO_2 were completely dissolved into the aqueous solution, the temperature was then maintained for 30 min, and the sample chamber was subsequently cooled at a rate of 1 °C/min. In situ cassiterite crystallization in the sample chamber was observed and recorded, including the crystal habit, initial and final crystallization temperatures, and growth rates. The vapor bubble-disappearing temperature, measured for the vapor bubble generated during cooling process in the sample chamber, was used to approximate the bulk density of the aqueous solution based on the equation of the state of H_2O (Wagner and Pruβ 2002) due to the low solubility of Li_2CO_3 in water (Anderson et al. 2001). The pressure in the sample chamber at any temperature during the experiment could subsequently be obtained along the isochore of this bulk density, assuming a constant volume of the sample chamber during the experiments (Shen et al. 1992; Bassett et al. 1993; Chou 2003; Schmidt and Chou 2012; Li et al. 2016). According to the data presented by Schmidt (2014), the true pressure in the alkali carbonate aqueous solution in the sample chamber is higher than that calculated in the way described above. Consequently, the pressure values obtained in this study can be considered as minima at certain temperatures. In addition, comparative experiments were performed using the same initial samples under different pressure conditions in the SnO_2–Li_2CO_3–H_2O system. A proper amount of water was drained from the chamber at room temperature without unloading the sample by loosening the driver screws upon the completion of one crystallization experiment. This decreased the bulk water density in the

sample chamber, such that the pressure within the sample chamber was lowered at any specified temperature during the reheating process along the new isochore. The aforementioned experimental procedures were then repeated to investigate the effect of pressure on cassiterite crystallization.

For the SnO_2–Na_2CO_3–H_2O experiments, a sintered SnO_2 lump, Na_2CO_3 powder, and distilled water were loaded into the HDAC sample chamber at room temperature, and the same experimental procedures outlined for the SnO_2–Li_2CO_3–H_2O experiments were employed. Because there are no equations of state for Na_2CO_3–H_2O, the pressure within the HDAC sample chamber cannot be obtained during the SnO_2–Na_2CO_3–H_2O experiments. Moreover, to determine the dissolution mechanism of SnO_2 in the alkali carbonate aqueous solution, the experiments in the SnO_2–H_2O and SnO_2–NaOH–H_2O systems were conducted using similar experimental procedures as those described for the SnO_2–Li_2CO_3–H_2O system.

To calculate the initial mass of SnO_2 and estimate the growth rates, the length and width of the cassiterite crystal were measured in the crystallization experiments through observation under an Olympus microscope, with an error of ±1 μm via repeated measurements. Subsequently, the volume of cassiterite was calculated, assuming that it had a square-column shape with equal width and thickness. The crystal mass of cassiterite was approximated based on the density (6.95 g/cm^3) of cassiterite. Similarly, the initial mass of Li_2CO_3 was approximated based on the product of the density (2.11 g/cm^3) and the volume of compacted Li_2CO_3 powder (approximated as spheres), which was calculated by measuring the diameters under the microscope. The mass of H_2O loaded into the HDAC sample chamber was obtained, which was based on the H_2O density calculated on the homogenization temperature of the aqueous solution in the chamber and the chamber volume that subtracted the volume of SnO_2 and Li_2CO_3.

To determine the species of dissolved SnO_2 in the alkali carbonate aqueous solution, in situ Raman analysis was performed in the SnO_2–Na_2CO_3–H_2O, SnO_2–Li_2CO_3–H_2O experiments and in the comparative experiments of Na_2CO_3–H_2O, SnO_2–NaOH–H_2O systems. Each Raman spectrum was acquired using a JY Horiba LabLam HR Raman system with a long working-distance Olympus 50× SLMP objective (numeral aperture 0.35). Analyses were performed using a 532-nm laser for excitation (~40 mW at the sample), a grating of 600 lines/mm, and a confocal pinhole diameter of 100 μm. All Raman spectra were recorded with two accumulations of 60 s each.

EXPERIMENTAL RESULTS

SnO_2 dissolution and crystallization

We conducted 21 experiments in the SnO_2–Li_2CO_3–H_2O system and 11 experiments in the SnO_2–Na_2CO_3–H_2O system (Tables 1 and 2). Five groups of comparative experiments in the SnO_2–Li_2CO_3–H_2O system were conducted (Nos. 1, 7, 8, 9, and 13 in Table 1), with the experiments in each group conducted using different bulk water densities for the same samples. The amounts of each component in these experiments are presented in Table 1. The unidirectional and volumetric growth rates of cassiterite were estimated for the experiments in which only one main crystal nucleated and grew (Tables 1 and 2).

In the SnO_2–Li_2CO_3–H_2O experiments, Li_2CO_3 melted first, forming melt droplets in the sample chamber during the heating process (Fig. 1b). Subsequently, SnO_2 dissolved in the aqueous solution (Figs. 1c and 1d). During the following cooling process, cassiterite nucleated and grew into long prismatic crystals in the 654–856 °C and 660–864 MPa temperature and pressure ranges, respectively (Fig. 1e); crystal growth stopped at 560–768 °C and 246–764 MPa

(Figs. 1e–1h). The Li_2CO_3 melt droplets appeared and increased in size during the cassiterite crystallization, until rapid zabuyelite crystallization at 515–614 °C in tabular shape and occasionally spherulite (Figs. 1f–1i). In the SnO_2–Na_2CO_3–H_2O experiments, SnO_2 dissolved in the Na_2CO_3 aqueous solution during heating. Long prismatic cassiterite crystals began to grow at 476–753 °C during the cooling process, and crystal growth ended at 390–619 °C (Fig. 2). Raman spectroscopic analysis revealed that the long prismatic crystals (Figs. 1h and 2c) were cassiterite (Fig. 3).

By plotting the crystal volume versus time, it was determined that the growth progress of cassiterite in the SnO_2–Li_2CO_3–H_2O and SnO_2–Na_2CO_3–H_2O systems is divided into three segments: initial stage of unobstructed growth, steady growth, and slow growth in the late stage (Fig. 4). In the SnO_2–Li_2CO_3–H_2O and SnO_2–Na_2CO_3–H_2O systems, cassiterite initially grew quickly with average rates of 111.23 and 80.09 $\mu m^3/s$, respectively (Interval A in Fig. 4). Subsequently, the plotted volumes versus time followed linear trends in the two systems (Interval B in Fig. 4), which indicated constant volumetric growth rates of 15.77 and 17.31 $\mu m^3/s$, respectively. Finally, the volume growth rates slowed down by one order of magnitude to 3.01 and 1.88 $\mu m^3/s$, respectively (Interval C in Fig. 4). Notably, the growth of larger crystals was frequently accompanied by the dissolution of smaller crystals during the cassiterite crystallization process, indicating the occurrence of Ostwald ripening (Fig. 5) (Thomas and Davidson 2016).

The SnO_2–H_2O experiments showed that the solubility of SnO_2 was very limited in water; thus, cassiterite crystal was not formed during the experiment. In contrast, SnO_2 exhibited significant solubility in the SnO_2–NaOH–H_2O system when heated to 300–600 °C. However, cassiterite did not crystallize during the subsequent cooling process.

In situ Raman analysis

In the SnO_2–Na_2CO_3–H_2O experiments (Fig. 6), the Raman spectrum of the aqueous solution exhibited an intense CO_3^{2-} peak at 1065 cm^{-1} and a weak HCO_3^- peak at 1017 cm^{-1} at 24 °C (Hurai et al. 2015), and the CO_3^{2-} peak shifted to lower wavenumbers as the temperature increased, similar to the Raman spectroscopy features for a Na_2CO_3–H_2O system (Rudolph et al. 2008; Schmidt 2014). A peak at ~971 cm^{-1} emerged in the Raman spectrum of the aqueous solution at 700 °C, shifting to lower wavenumbers with increasing temperature; a weak peak at 332 cm^{-1} appeared at 850 °C. Raman peaks at 332, 919, 971, 1017 (HCO_3^-) and 1065 cm^{-1} (CO_3^{2-}) were detected in the aqueous solution after cooling to 24 °C as well as in the Na_2CO_3–H_2O experiment (Fig. 6). The Raman peaks at 332, 919, and 971 cm^{-1} can be attributed to the tetrahedral ReO_4^- that formed during the reaction of alkali carbonate aqueous solution with the rhenium gasket at high temperature (Eysel and Kanellakopulos 1993; Chellappa et al. 2009; Foustoukos and Mysen 2015). The addition of a certain amount of rhenium did not appear to interfere with the crystallization kinetics of cassiterite in the alkali carbonate aqueous solutions.

In the SnO_2–Li_2CO_3–H_2O experiments (Fig. 7), the Raman peaks of ReO_4^- at 332, 919, and 971 cm^{-1} were clearly detected in the aqueous solution at 850 °C, in addition to the CO_3^{2-} peak at ~1065 cm^{-1} while a significant dissolution of Li_2CO_3 into water occurred at 600 °C. In addition to a weak peak at ~971 cm^{-1}, CO_3^{2-} peaks at ~1072 cm^{-1} (ν_1, the symmetric stretching vibration) and ~702 cm^{-1} (ν_4, the in-plane symmetric vibration) were observed in the Raman spectra of the Li_2CO_3 melt droplet (Bates et al. 1972; Carper et al. 2012; Foustoukos and Mysen 2015).

In the SnO_2–NaOH–H_2O experiments (Fig. 8), a Raman peak at ~552 cm^{-1} was detected at 300 °C after SnO_2 dissolution into the aqueous solution. During further heating, this peak

207 slightly shifted to lower wavenumbers, and the intensity significantly decreased. At 800 °C, the
208 ReO_4^- Raman peaks at 332, 919, and 971cm^{-1} were detected. All of the aforementioned peaks
209 remained in the Raman spectrum after cooling to 24 °C (Fig. 8).
210

211 **DISCUSSION**

212 **Tin speciation dissolved in alkali carbonate-rich aqueous solution**

213 SnO_2 is soluble in the SnO_2–Li_2CO_3–H_2O and SnO_2–Na_2CO_3–H_2O systems, and
214 cassiterite crystallization occurred during cooling (Figs. 1 and 2). This result differed from the
215 low solubility in water, as indicated in the experiments for the SnO_2–H_2O system. These results
216 indicated that the presence of alkali carbonate can enhance the solubility of SnO_2 in an aqueous
217 solution.

218 The hydrolysis of alkali carbonate in aqueous solutions can produce an alkaline
219 condition, as indicated by the presence of HCO_3^- in the SnO_2–Na_2CO_3–H_2O system (Fig. 6)
220 (Rudolph et al. 2008):

221 $CO_3^{2-} + H_2O = HCO_3^- + OH^-$ (1).

222 Under high pressure and temperature, the dissolved Sn(IV), as an amphoteric metal element,
223 should be present in an alkaline aqueous solution as $Sn(OH)_6^{2-}$ (Jackson and Helgeson 1985;
224 Lothenbach 1999; Rai et al. 2011):

225 $SnO_2 + 2OH^- + 2H_2O = Sn(OH)_6^{2-}$ (2).

226 However, in the SnO_2–Na_2CO_3–H_2O and SnO_2–Li_2CO_3–H_2O experiments, the Raman signal
227 from dissolved Sn(IV) was not detected, and only Raman peaks of CO_3^{2-} (1065 cm^{-1}), HCO_3^-
228 (1017 cm^{-1}), and ReO_4^- (332, 919, and 971 cm^{-1}) were present (Figs. 6 and 7). On the other
229 hand, in the SnO_2–NaOH–H_2O experiments, when SnO_2 was dissolved in the alkaline aqueous

solution by the reaction of Eq. 2, a Raman peak at 552 cm^{-1} was detected, which was assigned to ν_1[Sn(IV)–OH] of $Sn(OH)_6^{2-}$, as reported by Taylor and Coddington (1992). The intensity of the peak at 552 cm^{-1} significantly decreased with an increase in temperature (Fig. 8), which can be caused by the Sn(IV)–OH bonds in $Sn(OH)_6^{2-}$ becoming less polarizable at high temperatures (Schmidt 2014). The dissolution temperature of SnO_2 in the SnO_2–NaOH–H_2O system was much lower than that in the SnO_2–Li_2CO_3–H_2O and SnO_2–Na_2CO_3–H_2O systems, which indicated the higher solubility of SnO_2 in the SnO_2–NaOH–H_2O system. Thus, the weak polarization at high temperature and lower solubility of SnO_2 may not allow to detect the Raman spectrum of $Sn(OH)_6^{2-}$ at ~552 cm^{-1} in the SnO_2–Na_2CO_3–H_2O and SnO_2–Li_2CO_3–H_2O experiments, wherein SnO_2 dissolved into the alkaline aqueous solution as $Sn(OH)_6^{2-}$ with low concentrations at temperatures higher than 700 °C (Figs. 6 and 7). It could also be the reason that the Raman peak of HCO_3^- was not detected at high temperature in SnO_2–Na_2CO_3–H_2O and SnO_2–Li_2CO_3–H_2O experiments, as suggested from the Raman data by Schmidt (2014). Therefore, we inferred that Sn(IV) dissolved in alkali carbonate aqueous solutions as $Sn(OH)_6^{2-}$ under high pressure and temperature, rather than as a complex with carbonate such as Sn(IV) hydroxycarbonate (Kuril'chikova and Barsukov 1971; Kosals 1976). According to Eqs. 1 and 2, the dissolution of SnO_2 in an alkali carbonate aqueous solution can be expressed as the following reaction:

$$SnO_2 + 2CO_3^{2-} + 4H_2O = SnOH_6^{2-} + 2HCO_3^- \quad (3).$$

The roles of alkali carbonate in the solubility of SnO_2 can be attributed to the alkaline nature of carbonate aqueous solutions. The back reaction of Eq. 3 to cassiterite + CO_3^{2-} + H_2O occurred upon cooling. In contrast, the dissolution reaction of SnO_2 in the strong alkaline SnO_2–NaOH–H_2O system (Eq. 2) was not reversible and did not result in cassiterite crystallization during the cooling process. This indicates that strong alkaline conditions are unfavorable for the

crystallization of cassiterite, while the alkali carbonate aqueous solution provides suitable alkaline conditions for cassiterite crystallization.

The moles fraction of cassiterite crystallized from the SnO_2–Li_2CO_3–H_2O system ranges from 0.03 to 0.41 mol%, which mirrors the solubility of SnO_2 in aqueous solution (Table 1). Under certain ranges of temperatures and pressures (e.g., at approximately 700–800 °C and 700–800 MPa), the mole fraction of cassiterite crystallized from the aqueous solution is linearly related to the mole fraction of Li_2CO_3 dissolved in aqueous solution (Fig. 9). This suggests that the solubility of SnO_2 depends on the content of Li_2CO_3 in the aqueous solution, further indicating the effect of alkalinity, produced by the hydrolysis of alkali carbonate, on the solubility of SnO_2 in the hydrothermal fluids.

Cassiterite crystallization conditions and behaviors

The cassiterite crystallization occurred at 560–856 °C and approximately 246–864 MPa in the SnO_2–Li_2CO_3–H_2O system and primarily ended at rare metal pegmatite-forming P–T conditions (Table 1 and Fig. 10a). This temperature condition is higher than that (390–753 °C) in the SnO_2–Na_2CO_3–H_2O system (Table 2). It can be because of the low solubility of Li_2CO_3 that led to the relatively low solubility of SnO_2 in the aqueous solution. Therefore, if more soluble alkali carbonates (e.g., Na_2CO_3) dissolve in the aqueous solution, the crystallization P–T conditions of cassiterite will be lower and much closer to the rare metal pegmatite-forming P–T conditions (Fig. 10a). This finding is consistent with the enrichment of Li^+, Na^+, K^+, CO_2, CO_3^{2-}, and HCO_3^- in the melt and fluid inclusions of many tin-mineralized pegmatites (Rickers et al. 2006; Thomas et al. 2006a, 2012; Thomas and Davidson 2016). In some cases, the concentrations of carbonates and bicarbonates can achieve as high as 20–40 wt% (Thomas et al.

2006b). Therefore, the P–T conditions of cassiterite crystallization in alkali carbonate-rich environment can reflect the cassiterite crystallization conditions in the rare metal granitic pegmatite.

In each of the five groups of comparison experiments in the SnO_2–Li_2CO_3–H_2O system, both the initiation and ending temperatures of cassiterite crystallization increased with pressure decreasing (Table 1 and Fig. 10b). This negative P–T trend of cassiterite crystallization can reflect the effect of pressure on SnO_2 solubility, which was in contrast to the data presented by Wilson and Eugster (1990) and Schmidt (2018) that showed that the effect of pressure on SnO_2 solubility in H_2O+HCl is insignificant.

Growth rates in the order of 1 cm per 1000–10,000 years have been reported for K-feldspar crystals growing in granite (Pitcher 2012). Experimental studies on the kinetics of crystallization of hydrous granitic melts reported that the crystal growth rates were in the order of 10^{-6}–10^{-8} cm/s (Fenn 1977; Swanson and Fenn 1992; Baker and Freda 2001; Li et al. 2013; Sirbescu et al. 2017; Maneta and Anderson 2018). These growth rates are equivalent to or lower than the average length growth rates (0.61×10^{-6}–8.22×10^{-6} cm/s) of cassiterite in alkali carbonate aqueous solutions (Tables 1 and 2). The cassiterite volume versus time shows unobstructed and steady linear trends (Intervals A and B in Fig. 4). In this study, the average volume growth rates of cassiterite range from 3.40 to 19.07 $\mu m^3/s$ (Tables 1 and 2), which confirms to the values (10^{-5}–10^2 $\mu m^3/s$) measured for the undercooled pegmatitic melt (Sirbescu et al. 2017). The high growth rates indicate the low viscosity of alkali carbonate-rich aqueous solutions that enhances the diffusion of components and, therefore, speeds up the growth of the crystals (Thomas and Davidson 2016). Obvious Ostwald ripening that occurred in some experiments, also indicates the high diffusion of $Sn(OH)_6^{2-}$ in the alkali carbonate aqueous

299 solution because Ostwald ripening requires enough compositions to transfer to the cassiterite
300 crystallization front during the dissolution of finer cassiterite crystals (Thomas and Davidson
301 2016). As a result, the long prismatic cassiterite crystals formed in the sample chamber (Figs. 1h
302 and 2c) because the (110) prismatic surface of cassiterite with the lowest surface energy
303 preferentially grows while high diffusion supplies nutrition to the crystal surface (Smith et al.
304 1995; Batzill and Diebold 2005).
305
306 **Roles of carbonate in tin mineralization in granitic pegmatite conditions**
307 The HDAC sample chamber loaded with alkali carbonate-rich aqueous solution is similar
308 to the alkali carbonate-rich inclusions that represent the hydrous melt or fluid from which tin-
309 mineralized pegmatite crystallized (Thomas et al. 2011; Thomas and Davidson 2013). As
310 discussed above, the formation conditions of cassiterite can fall within the rare metal pegmatite-
311 forming P–T conditions if the alkali carbonates in aqueous solution are as rich as they are in
312 many pegmatite-forming melts or fluids. Moreover, in the alkali carbonate-rich tin-mineralized
313 pegmatites, cassiterite occurs in the form of long prismatic crystals that are similar to those
314 grown in the present experiments, such as the cassiterite from the peralkaline zones of the
315 Ehrenfriedersdorf pegmatites in 5-cm-long prismatic shapes (Thomas et al. 2006a). The long
316 prismatic shape of cassiterite indicates the high diffusion rate of Sn in pegmatitic melt or fluid
317 (Smith et al. 1995; Batzill and Diebold 2005), resulting in high growth rates of cassiterite in
318 pegmatite-forming conditions (Chakoumakos and Lumpkin 1990; Morgan and London 1999;
319 Webber et al. 1999; Sirbescu et al. 2009; Li et al. 2013). It is also consistent with the growth rate
320 of cassiterite in the carbonate-rich aqueous solution as mentioned above.

The above features indicate that carbonates can play important roles in the formation of tin mineralization in high-fractionated pegmatite enriched in lithium or sodium. The carbonate-rich aqueous solution has a high Sn(IV) transport capability in the form of $Sn(OH)_6^{2-}$ to the crystallization front of cassiterite, which helps to form long prismatic cassiterite macrocrystals during the pegmatite-forming process. This observation agrees with the experiments of Schmidt (2018), which showed that tin can be transported in Sn(IV). Moreover, alkali carbonates can lower the crystallization temperature and solidi, increase the crystallization rate (Sirbescu and Nabelek 2003) and decrease the viscosity of a hydrous melt by as much as 2–3 orders of magnitude (Ejima et al. 1987; Thomas et al. 2012; Jones et al. 2013; Thomas and Davidson 2016). These properties are essential for the formation of pegmatite texture (London 2009). Therefore, carbonate-rich silicate melts or highly concentrated fluids can serve as media for tin mineralization in granitic pegmatite (Thomas et al. 2011; Li and Chou 2017; Maneta and Anderson 2018).

IMPLICATIONS

The roles of suitable alkaline condition produced by alkali carbonates in tin mineralization can be extended to LCT-type pegmatite because many LCT pegmatites (e.g., Amis, Borborema, Bornholm, Elba, Froland, Königshain, Orlovka, Muiane, and Tanco) have plenty of alkali carbonate-rich inclusions (Thomas et al. 2011, 2012; Li and Chou 2016). Alkali carbonates occur as daughter crystals in crystal-rich inclusions, mainly including nahcolite [$NaHCO_3$], zabuyelite [Li_2CO_3], potash [K_2CO_3], and dawsonite [$NaAl(CO_3)(OH)_2$] in addition to the volatile phases (CO_2) and carbonates/bicarbonates dissolved in the aqueous solution (Thomas et al. 2012). These crystal-rich inclusions contain ~7 mol% Li_2CO_3 in the Tanco Li-Ta

pegmatite (Anderson 2001), 35.0 wt% $NaHCO_3$ in the Orlovka pegmatite in Russia (Thomas et al. 2011), and 10 vol% Li_2CO_3 in the Jiajika lithium pegmatite in China (Li and Chou 2016). In the crystal-rich inclusions hosted in spodumene in the Jiajika pegmatite, China (Li and Chou 2016), alkali carbonate can react with lithium aluminosilicate into soluble silicate or aqueous solution (Thomas et al. 2011; Li and Chou 2017). Similarly, alkaline conditions enhance the solubility of beryllium (Thomas et al. 2009) and tungsten (Li et al. 2018) in the form of ions (e.g., Be^{+} and W^{6+}) in a pegmatite melt or a fluid. The alkali carbonate-rich aqueous solution can also dissolve more SiO_2 and Al_2O_3 than pure water under pegmatite-forming P–T conditions (Ye et al. 2008; Schmidt 2014), which are essential components for granitic pegmatite formation (London 2008).

Moreover, an alkali carbonate-rich hydrous melt or fluid bears low crystallization temperature and solidi and low viscosity, which helps to form the boundary layer liquid in the "constitutional zone refining" pegmatite-forming model (London 2018). Carbonates promote the occurrence of immiscibility in alkaline-rich granitic magma (Veksler 2004; Linnen et al. 2014) in the pegmatite-forming model of immiscibility (Thomas and Davidson 2016). Consequently, CO_2 or carbonate could be types of fluxes to promote the formation of rare metal pegmatites, and alkali carbonate-rich aqueous solutions or hydrous melts are potential media for the formation of rare metal mineralization.

ACKNOWLEDGMENTS

This study was supported by the National Natural Science Foundation of China (41872096), the Chinese National Non-profit Institute Research Grant of CAGS-IMR

366 (JYYWF201814), the National Key R&D Program of China (2016YFC0600208), and the Key
367 Frontier Science Program (QYZDY-SSW-DQC008) of Chinese Academy of Sciences.

368

369 **REFERENCES CITED**

370 Anderson, A.J., Clark, A.H., and Gray, S. (2001) The occurrence and origin of zabuyelite
371 (Li_2CO_3) in spodumene-hosted fluid inclusions: Implications for the internal evolution of
372 rare-element granitic pegmatites. Canadian Mineralogist, 39, 1513–1527.

373 Audétat, A., Gunther, D., and Heinrich, C.A. (1998) Formation of a magmatic-hydrothermal ore
374 deposit: Insights with LA-ICP-MS analysis of fluid inclusions. Science, 279, 2091–2094.

375 Baker, D.R., and Freda, C. (2001) Eutectic crystallization in the undercooled orthoclase-quartz-
376 H_2O system: Experiments and simulations. European Journal of Mineralogy, 13, 453–466.

377 Bassett, W.A., Shen, A.H., Bucknum, M., and Chou, I-M. (1993) A new diamond anvil cell for
378 hydrothermal studies to 2.5 GPa and from –190 to 1200 °C. Review of Scientific
379 Instruments, 64, 2340–2345.

380 Bassett, W.A., Wu, T.C., Chou, I-M., Haselton, H.T. Jr., Frantz, Z., Mysen, B.O., Huang, W.L.,
381 Sharma, S.K., and Schiferl, D. (1996) The hydrothermal diamond anvil cell (HDAC) and its
382 applications. In M.D. Dyar, C. McCammon, and M.W. Schaefer, Eds., Mineral
383 Specptroscopy: A Tribute to Roger G. Burns, p. 261–272. The Geochemical Society, Special
384 Publication No. 5.

385 Bates, J.B., Brooker, M.H., Quist, A.S., and Boyd, G.E. (1972) Raman spectra of molten alkali
386 metal carbonates. The Journal of Physical Chemistry, 76, 1565–1571.

387 Batzill, M., and Diebold, U. (2005) The surface and materials science of tin oxide. Progress in
388 Surface Science, 79, 47–154.

389 Bhalla, P., Holtz, F., Linnen, R.L., and Behrens, H. (2005) Solubility of cassiterite in evolved
390 melts: Effect of T, fO_2, and additional volatiles. Lithos, 80, 387–400.
391 Carper, W.R., Wahlbeck, P.G., and Griffiths, T.R. (2012) DFT models of molecular species in
392 carbonate molten salts. Journal of Physical Chemistry B, 116, 5559–5567.
393 Chakoumakos, B.C., and Lumpkin, G.R. (1990) Pressure-temperature constraints on the
394 crystallization of the Harding pegmatite, Taos country, New Mexico. Canadian Mineralogist,
395 28, 287–298.
396 Chellappa, R.S., Somayazulu, M., and Hemley, R.J. (2009) Rhenium reactivity in H_2O–O_2
397 supercritical mixtures at high pressures. High Pressure Research, 29, 792–799.
398 Chou, I-M. (1996) Precautions on the use of the hydrothermal diamond-anvil cell for the
399 acquisition of volumetric and phase relation data of geologic fluids. PACROFI VI, Program
400 and Abstracts, p. 31.
401 Chou, I-M. (2003) Hydrothermal diamond-anvil cell: application to studies of geologic fluids.
402 Acta Petrologica Sinica, 19, 213–220.
403 Duc-Tin, Q., Audétat, A., and Keppler, H. (2007) Solubility of tin in (Cl, F)-bearing aqueous
404 fluids at 700 °C, 140 MPa: A LA-ICP-MS study on synthetic fluid inclusions. Geochimica et
405 Cosmochimica Acta, 71, 3323–3335.
406 Ejima, T., Sato, Y., Yamamuro, T., Tamai, K., Hasebe, M., Bohn, M.S., and Janz, G.J. (1987)
407 Viscosity of the eutectic Li_2CO_3–Na_2CO_3–K_2CO_3 melt. Journal of Chemical & Engineering
408 Data, 32, 180–182.
409 Eysel. H.H., and Kanellakopulos, B. (1993) Raman spectra, absolute Raman intensities and
410 electro-optical parameters of pertechnetate, perrhenate and periodate ions in aqueous
411 solution. 24, 119–122.

412 Fenn, P.M. (1977) The nucleation and growth of alkali feldspars from hydrous melts. Canadian
413 Mineralogist, 15, 135–161.
414 Foustoukos, D.I., and Mysen, O.B. (2015) The structure of water-saturated carbonate melts.
415 American mineralogist, 100, 35–46.
416 Fu, M., and Kwak, T.A.P. (1994) Geology, geochemistry and fluid inclusions of the Gejiu tin-
417 polymetallic field, People's Republic of China. International Geology Review, 36, 272–292.
418 Fu, M., Kwak, T.A.P., and Mernagh, T.P. (1993) Fluid inclusions studies of zoning in the
419 Dachang tin-polymetallic ore field, the People's Republic of China. Economic Geology, 88,
420 283–300.
421 Heinrich, C.A. (1990) The chemistry of hydrothermal tin (-tungsten) ore deposition. Economic
422 Geology, 85, 457–481.
423 Hurai, V., Huraiová, M., Slobodník, M., and Thomas, R. (2015) Geofluids: Developments in
424 Microthermometry, Spectroscopy, Thermodynamics and Stable Isotopes, 504 p. Elsevier.
425 Jackson, K.J., and Helgeson, H.C. (1985) Chemical and thermodynamic constraints on the
426 hydrothermal transport and deposition of tin: I. Calculation of the solubility of cassiterite at
427 high pressures and temperatures. Geochimica et Cosmochimica Acta, 49, 1–22.
428 Jones, A.P., Genge, M., and Carmody, L. (2013) Carbonate melts and Carbonatites. Reviews in
429 Mineralogy and Geochemistry, 75, 289–322.
430 Kamilli, R.J., Kimball, B.E., and Carlin, J.F. Jr. (2017) Chapter S. Tin. In K.J. Schulz, J.H. Jr.
431 DeYoung, R.R. II Seal, and D.C. Bradley, Eds., Critical Mineral Resources of The United
432 States—Economic and Environmental Geology and Prospects for Future Supply, p. S1–S53.
433 U.S. Geological Survey Professional Paper 1802, Reston, VA.

434 Kokh, M.A., Akinfive, N.N., Pokrovski, G.S., Salvi, S., and Guillaume, D. (2017) The role of
435 carbon dioxide in the transport and fractionation of metals by geological fluids. Geochimica
436 et Cosmochimica Acta, 197, 433–466.
437 Korges, M., Weis, P., Lüders, V., and Laurent, O. (2018) Depressurization and boiling of a single
438 magmatic fluid as a mechanism for tin-tungsten deposit formation. Geology 46, 75–78.
439 Kosals, J.A. (1976) Main Features of Geochemistry of Rare Metals in Granitic Melts and
440 Solutions (Fluids), 232 p. Nauka, Novosibirsk (in Russian).
441 Kuril'chikova, G.Y., and Barsukov, V.L. (1971) Effects of CO_2 and of sodium and potassium
442 bicarbonates and carbonates on the formation of Sn (IV) complexes in solution.
443 Geochemical International, 8, 395–404.
444 Li, T.J. (1989) Experimental studies of the solubility of cassiterite and the extraction of tin from
445 granitic melts. Chinese Journal of Geochemistry, 8, 84–96.
446 Li, J.K., and Chou, I-M. (2016) An occurrence of metastable cristobalite in spodumene-hosted
447 crystal-rich inclusions from Jiajika pegmatite deposit, China. Journal of Geochemical
448 Exploration, 2016, 29–36.
449 Li, J.K., and Chou, I-M. (2017) Homogenization experiments of crystal-rich inclusions in
450 spodumene from Jiajika lithium deposit, china, under elevated external pressures in a
451 hydrothermal diamond-anvil cell. Geofluids, 2017, 1–12.
452 Li, J.K., Chou, I-M., Yuan, S.D., and Burruss, R.C. (2013) Observations on the crystallization of
453 spodumene from aqueous solutions in a hydrothermal diamond-anvil cell. Geofluids, 13,
454 467–474.
455 Li, J.K., Bassett, W.A., Chou, I-M., Ding, X., Li, S.H., and Wang, X.Y. (2016) An improved
456 hydrothermal diamond anvil cell. Review of Scientific Instruments, 87, 1513–1527.

457 Li, J.K, Liu, Y.C., Zhao, Z., and Chou, I-M. (2018) Roles of carbonate/CO_2 in the formation of
458 quartz-vein wolframite deposits: Insight from the crystallization experiments of huebnerite
459 in alkali-carbonate aqueous solutions in a hydrothermal diamond-anvil cell. Ore Geology
460 Reviews. 95, 40–48.
461 Linnen, R.L. (1998) Depth of emplacement, fluid provenance and metallogeny in granitic
462 terrains: A comparison of western Thailand with other Sn-W belts. Mineralium Deposita, 33,
463 461–476.
464 Linnen, R.L., Pichavant, M., Holtz, F., and Burgess, S. (1995) The effect of fO_2 on the solubility,
465 diffusion, and speciation of tin in haplogranitic melt at 850 °C and 2 kbar. Geochimica et
466 Cosmochimica Acta, 59, 1579–1588.
467 Linnen, R.L., Samson, I.M., Williams-Jones, A.E., and Chakhmouradian, A.R. (2014)
468 Geochemistry of the rare-earth element, Nb, Ta, Hf, and Zr Deposits. In K.K. Turekian, and
469 H.D. Holland, Eds., Treatise on Geochemistry (Second Edition), p. 543–568. Elsevier,
470 Oxford.
471 London, D. (2008) Pegmatites, 368 p. Canadian Mineralogist Special Publication, 10.
472 London, D. (2009) The origin of primary textures in granitic pegmatites. Canadian Mineralogist,
473 47, 697–724.
474 London, D. (2018) Ore-forming processes within granitic pegmatites. Ore Geology Reviews,
475 101, 349–383.
476 Lothenbach, B., Ochs, M., Wanner, H., and Yui, M. (1999) Thermodynamic date for the
477 speciation and solubility of Pd, Pb, Sn, Sb, Nb, and Bi in aqueous solution. 340 p. JNC
478 Report TN8400 99-011, Japan.

Maneta, V., and Anderson, A.J. (2018) Monitoring the crystallization of water-saturated granitic melts in real time using the hydrothermal diamond anvil cell. Contributions to Mineralogy and Petrology, 173, 83.

Morgan, G.B., and London, D. (1999) Crystallization of the Little Three layered pegmatite-aplite dike, Ramona District, California. Contributions to Mineralogy and Petrology, 136, 310–330.

Müller, B., and Seward, T.M. (2001) Spectrophotometric determination of the stability of tin (II) chloride complexes in aqueous solution up to 300 °C. Geochimica et Cosmochimica Acta, 65, 4187–4199.

Naumov, V.B., Dorofeev, V.A., and Mironova, O.F. (2011) Physicochemical parameters of the formation of hydrothermal deposits: A fluid inclusion study. I. Tin and tungsten deposits. Geochemistry International, 49, 1063–1082.

Phillips, G.N., and Evans, K.A. (2004) Roles of CO_2 in the formation of gold deposits. Nature 429, 860–863.

Pitcher, W.S. (2012) The Nature and Origin of Granite, 2nd ed., 387 p. Springer Science & Business Media, Dordrecht, Netherlands.

Rai, D., Yui, M., Todd Schaef, H., and Kitamura, A. (2011) Thermodynamic model for SnO_2(cr) and SnO_2(am) solubility in the aqueous Na^+–H^+–OH^-–Cl^-–H_2O system. Journal of Solution Chemistry, 40, 1155–1172.

Rickers, K., Thomas, R., and Heinrich, W. (2006) The behavior of trace elements during the chemical evolution of the H_2O-, B-, and F-rich granite–pegmatite–hydrothermal system at Ehrenfriedersdorf, Germany: A SXRF study of melt and fluid inclusions. Mineralium Deposita, 41, 229–245.

Rudolph, W.W., Irmer, G., and Königsberger, E. (2008) Speciation studies in aqueous HCO_3^-–CO_3^{2-} solutions. A combined Raman spectroscopic and thermodynamic study. Dalton Transactions, 2008, 900–908.

Schmidt, C. (2014) Raman spectroscopic determination of carbon speciation and quartz solubility in H_2O+Na_2CO_3 and H_2O+$NaHCO_3$ fluids to 600 °C and 1.53 GPa. Geochimica et Cosmochimica Acta, 145, 281–296.

Schmidt, C. (2018) Formation of hydrothermal tin deposits: Raman spectroscopic evidence for an important role of aqueous Sn (IV) species. Geochimica et Cosmochimica Acta, 220, 499–511.

Schmidt, C., and Chou, I-M. (2012) The hydrothermal diamond anvil cell (HDAC) for Raman spectroscopic studies of geological fluids at high pressures and temperatures. In J. Dubessy, M.C. Caumon, and F. Rull, Eds., Raman Spectroscopy Applied to Earth Science and Cultural Heritage, 12, 247–276. EMU Notes in mineralogy, Aberystwyth, UK.

Shaposhnikov, V.V., and Aranovich, L.Y. (2015) Experimental study of model granite melting in the presence of alkali carbonate solutions at 400 MPa. Geochemistry International, 53, 838–844.

Shen, A.D., Bassett, W.A., and Chou, I-M. (1992) Hydrothermal studies in a diamond anvil cell: pressure determination using the equation of state. In Y. Syono, and M.H. Manghnani, Eds., High-pressure Research: Application to Earth and Planetary Sciences, p. 61–68. American Geophysical Union, Washington.

Sherman, D.M., Ragnarsdottir, K.V., Oelkers, E.H., and Collins, C.R. (2000) Speciation of tin (Sn^{2+} and Sn^{4+}) in aqueous Cl solutions from 25 °C to 350 °C: An in situ EXAFS study. Chemical Geology, 167, 169–176.

525 Sirbescu, M.C., and Nabelek, P.I. (2003) Crustal melts below 400 °C. Geology, 31, 685–688.
526 Sirbescu, M.C., Wilke, M., and Veksler, I.V. (2009) Understanding pegmatite texture: Kinetics of
527 crystallization in the haplogranite-Li-B-H_2O system. American Geophysical Union, 90,
528 V43B–2233.
529 Sirbescu, M.C., Schmidt, C., Veksler, I.V., Whittington, A.G., and Wilke, M. (2017)
530 Experimental crystallization of undercooled felsic liquids: Generation of pegmatitic texture.
531 Journal of Petrology, 58, 539–568.
532 Smith, A., Laurent, J.M., Smith, D.S., Bonnet, J.P., and Clemente, R.R. (1995) Structural and
533 electrical studies on highly conducting spray deposited fluorine and antimony doped SnO_2
534 thin films from $SnCl_2$ precursor. Thin Solid Films, 266, 20–30.
535 Štemprok, M. (1990) Solubility of tin, tungsten and molybdenum oxides in felsic magmas.
536 Mineralium Deposita, 25, 205–212.
537 Swanson, S.E., and Fenn, P.M. (1992) The effect of F and Cl on the kinetics of albite
538 crystallization: A model for granitic pegmatites? Canadian Mineralogist, 30, 549–559.
539 Taylor, J.R., and Coddington, J.M. (1992) The constitution of aqueous tin(IV) chloride and
540 bromine solutions and solvent extracts studied by ^{119}Sn NMR and vibrational spectroscopy.
541 Polyhedron, 11, 1531–1544.
542 Taylor, J.R., and Wall, V.J. (1993) Cassiterite solubility, tin speciation, and transport in a
543 magmatic aqueous phase. Economic Geology, 88, 437–460.
544 Thomas, R., and Davidson, P. (2012) Water in granite and pegmatite-forming melts. Ore Geology
545 Reviews, 46, 32–46.
546 Thomas, R., and Davidson, P. (2013) The missing link between granites and granitic pegmatites.
547 Journal of Geosciences, 58, 183–200.

548 Thomas, R., and Davidson, P. (2016) Revisiting complete miscibility between silicate melts and
549 hydrous fluids, and the extreme enrichment of some elements in the supercritical state—
550 Consequences for the formation of pegmatites and ore deposits. Ore Geology Reviews, 72,
551 1088–1101.
552 Thomas, R., Webster, J.D., Rhede, D., Seifert, W., Rickers, K., Förster, H.J., Heinrich, W., and
553 Davidson, P. (2006a) The transition from peraluminous to peralkaline granitic melts:
554 Evidence from melt inclusions and accessory minerals. Lithos, 91, 137–149.
555 Thomas, R., Webster, J.D., and Davidson, P. (2006b) Understanding pegmatite formation: The
556 melt and fluid inclusion approach. Mineralogical Association Canada Short Course, 36,
557 189–210.
558 Thomas, R., Davidson, P., and Badanina, E. (2009) A melt and fluid inclusion assemblage in
559 beryl from pegmatite in the Orlovka amazonite granite, East Transbaikalia, Russia:
560 implications for pegmatite-forming melt systems. Mineralogy and Petrology, 96, 129–140.
561 Thomas, R., Davidson, P., and Schmidt, C. (2011) Extreme alkali bicarbonate- and carbonate-
562 rich fluid inclusions in granite pegmatite from the Precambrian Rønne granite, Bornholm
563 Island, Denmark. Contributions to Mineralogy and Petrology, 161, 315–329.
564 Thomas, R., Davidson, P., and Beurlen, H. (2012) The competing models for the origin and
565 internal evolution of granitic pegmatites in the light of melt and fluid inclusion research.
566 Mineralogy and Petrology, 106, 55–73.
567 Veksler, I.V. (2004) Liquid immiscibility and its role at the magmatic–hydrothermal transition: a
568 summary of experimental studies. Chemical Geology, 210, 7–31.

569 Wagner, W., and Pruβ, A. (2002) The IAPWS formulation 1995 for the thermodynamic
570 properties of ordinary water substance for general and scientific use. Journal of Physical and
571 Chemical Reference Data, 31, 387–535.
572 Webber, K.L., Simmons, W.B., Falster, A.U., and Foord, E.E. (1999) Cooling rates and
573 crystallization dynamics of shallow level pegmatite–aplite dikes, San Diego County,
574 California. American Mineralogist, 84, 708–717.
575 Wilson, G.A., and Eugster, H.P. (1990) Cassiterite solubility and tin speciation in supercritical
576 chloride solutions. Geochemistry Society Special Publication, 2, 179–195.
577 Xiong, X., Li, J.K., Wang, D.H., Li, S.P., and Lin, H. (2019) Fluid characteristics and evolution
578 of the Zhawulong granitic pegmatite lithium deposit in the Ganzi-Songpan region,
579 Southwestern China. Acta Geologica Sinica (English Edition), 93, 943–954.
580 Ye, Y.P., Zeng, X.Q., Qian, W.L., and Wang, M.W. (2008) Synthesis of pure zeolites from
581 supersaturated silicon and aluminum alkali extracts from fused coal fly ash. Fuel, 87, 1880–
582 1886.
583

This is a preprint, the final version is subject to change, of the American Mineralogist (MSA)
Cite as Authors (Year) Title. American Mineralogist, in press.
DOI: https://doi.org/10.2138/am-2020-7118

584 **Figure captions**

585

586 Figure 1. Images from experiment No. 7-1 (Table 1) taken at various temperatures. The pressures
587 marked on the lower right corners represent minimum values in the sample chamber at
588 corresponding temperatures, because the true pressure is higher than that calculated based on the
589 equation of state of H_2O (Schmidt 2014). (a) The sample chamber was loaded with SnO_2,
590 Li_2CO_3, distilled water, and vapor bubbles at room temperature (24 °C). (b) Li_2CO_3 melted in the
591 water with increasing temperature, forming melt droplets at 639 °C. (c) SnO_2 was dissolving in
592 aqueous solution at 724 °C. (d) SnO_2 has almost completely dissolved in the aqueous solution at
593 766 °C. (e) Cassiterite nucleated and grew on the wall of the sample chamber during 1 °C/min
594 cooling, at 741 °C. (f) Li_2CO_3 exsolved from aqueous solution and formed melt droplets during
595 the cassiterite crystallization process at 727 °C. (g) The Li_2CO_3 melt droplets became larger
596 during further cooling. (h) Cassiterite growth ended at 660 °C. (i) Zabuyelite crystallized at 525
597 °C.

598

599 Figure 2. Images from experiment No. 11 (Table 2) taken at various temperatures. (a) Cassiterite
600 nucleation and growth during 1 °C/min cooling, at 753 °C. (b) Cassiterite growth as long
601 prismatic crystals. (c) Cessation of cassiterite growth at 619 °C.

602

603 Figure 3. Raman spectra of cassiterite crystallized in the systems of SnO_2–Li_2CO_3–H_2O (a),
604 SnO_2–Na_2CO_3–H_2O (b), and from the RRUFF database (c, RRUFF ID: R040017).

605

606 Figure 4. Representative volumetric growth rate diagram for cassiterite in the SnO_2–Li_2CO_3–H_2O
607 and SnO_2–Na_2CO_3–H_2O systems. Note, that the time was set to 0 s when the first measurement
608 was performed once the crystal appeared. The solid lines represent regression fit curves. For both
609 SnO_2–Li_2CO_3–H_2O and SnO_2–Na_2CO_3–H_2O systems, the volumetric growth rates of cassiterite
610 changed in three intervals. Interval A: unobstructed growth with the average rates of 111.23 and
611 80.09 $\mu m^3/s$, respectively. Interval B: steady growth with the rates of 15.77 and 17.31 $\mu m^3/s$,
612 respectively, which was obtained from the slopes of the linear regression fit curves. Interval C:
613 slow growth with the average rates of 3.01 and 1.88 $\mu m^3/s$, respectively.
614
615 Figure 5. Ostwald ripening phenomenon observed in experiment No. 3 (Table 1). (a) Formation
616 of different-sized cassiterite crystals in the sample chamber during 1 °C/min cooling, at 796 °C.
617 (b) Gradual growth of the larger crystals and dissolution of the smaller crystals at 792 °C. (c)
618 Complete dissolution of the smaller crystals and continued growth of the larger crystals at 775
619 °C.
620
621 Figure 6. Raman spectra of the aqueous solution measured at different temperatures in the SnO_2–
622 Na_2CO_3–H_2O and Na_2CO_3–H_2O experiments. The spectra colored in red and blue were obtained
623 in the SnO_2–Na_2CO_3–H_2O system during the heating and cooling processes, respectively. The
624 spectrum colored in black was obtained in the Na_2CO_3–H_2O system at 24 °C after cooling from
625 850 °C. The Raman peaks in the spectra are assigned to ReO_4^- (332, 919, and 971 cm^{-1}), HCO_3^-
626 (1017 cm^{-1}), and CO_3^{2-} (1065 cm^{-1}) (Eysel and Kanellakopulos 1993; Hurai et al. 2015). For
627 clarity, the spectra were shifted along the intensity axis.
628

Figure 7. Raman spectra of the aqueous solution and melt measured at different temperatures in the SnO_2–Li_2CO_3–H_2O experiment. The spectra colored in red and blue were obtained from the aqueous solution during the heating and cooling processes, respectively. The spectra colored in purple were obtained from the melt droplet coexisting with the aqueous solution during cooling process. The Raman peaks in the spectra are assigned to ReO_4^- (332, 919, and 971 cm^{-1}), CO_3^{2-} in aqueous solution (1065 cm^{-1}), and CO_3^{2-} in melt (~702 and ~1072 cm^{-1}) (Bates et al. 1972; Eysel and Kanellakopulos 1993; Carper et al. 2012; Hurai et al. 2015). For clarity, the spectra were shifted along the intensity axis.

Figure 8. Raman spectra of the aqueous solution in the SnO_2–NaOH–H_2O experiment measured during heating from 24 °C to 800 °C (in red color) and at 24 °C after cooling from 800 °C (in blue color). The Raman peaks in the spectra are assigned to ReO_4^- (332, 919, and 971 cm^{-1}) and $Sn(OH)_6^{2-}$ (552 cm^{-1}) (Taylor and Coddington 1992; Eysel and Kanellakopulos 1993). For clarity, the spectra were shifted along the intensity axis.

Figure 9. Mole fraction diagram of Li_2CO_3 and crystallized cassiterite in the SnO_2–Li_2CO_3–H_2O experiments. The experimental data under similar temperature and pressure conditions (approximately 700–800 °C and 700–800 MPa) were selected from Table 1, where the numbers represent the experimental numbers. The solid line represents the linear regression fit curve.

Figure 10. (a) Cassiterite crystallization conditions in the SnO_2–Li_2CO_3–H_2O system. The dashed lines show the pressure–temperature (P–T) paths of each experiment listed in Table 1. The gray area represents the formation conditions of rare element pegmatite proposed by London (2008).

652 (b) The P–T diagram of the five groups of comparative experiments in the SnO_2–Li_2CO_3–H_2O
653 system performed using the same initial samples under different pressure conditions were
654 marked with the experimental group numbers. The negative trends of the initiation and ending
655 P–T conditions of cassiterite crystallization in the same group of experiments were marked with
656 dotted lines, and overall P–T trends were indicated with thick gray arrows. In both (a) and (b),
657 the red circles and blue diamonds represent the crystallization-beginning and ending P–T
658 conditions, respectively.
659

Table 1. Experimental results of cassiterite crystallization in the SnO_2–Li_2CO_3–H_2O system.

[a]No.	[b]$m(SnO_2)$ (10^{-6} g)	[c]$m(Li_2CO_3)$ (10^{-6} g)	[d]$m(H_2O)$ (10^{-6} g)	[e]$x(SnO_2)$ (mol%)	[f]$x(Li_2CO_3)$ (mol%)	[g]T_h (°C)	[h]T_B (°C)	[i]T_S (°C)	[j]P_B (MPa)	[k]P_S (MPa)	[l]N	[m]v_{aveL} (10^{-6} cm/s)	[n]v_{aveV} (μm³/s)
1-1	0.66	2.32	30.59	0.25	1.81	225	824	631	864	602	1	0.62	8.20
1-2	0.66	2.32	26.46	0.29	2.08	281	833	750	642	552	1	8.22	19.07
1-3	0.66	2.32	24.91	0.31	2.21	290	856	768	628	537	3	[o]/	/
2	0.07	1.44	28.08	0.03	/	292	661	560	417	307	5	/	/
3	0.42	2.43	27.89	0.18	2.07	276	802	710	628	525	1	2.81	10.95
4	0.16	2.31	30.74	0.06	/	245	712	680	640	599	20	/	/
5	0.15	2.29	22.73	0.08	2.39	296	770	665	517	408	5	/	/
6	1.09	4.46	30.54	0.41	3.42	231	790	758	795	753	6	/	/
7-1	0.49	2.48	22.34	0.25	2.62	220	741	660	773	660	3	/	/
7-2	0.49	2.48	21.24	0.27	/	250	825	704	761	612	5	/	/
8-1	0.43	2.90	29.85	0.17	2.30	212	734	678	794	715	3	/	/
8-2	0.43	2.90	27.94	0.18	2.46	252	771	683	687	578	7	/	/
9-1	0.29	2.51	34.27	0.10	1.75	166	654	605	844	764	13	/	/
9-2	0.29	2.51	28.87	0.12	2.07	237	781	645	759	580	5	/	/
10	0.45	4.00	28.84	0.18	3.26	198	703	627	803	689	10	/	/
11	0.16	1.50	27.24	0.07	/	235	702	590	664	512	11	/	/
12	0.36	2.38	23.31	0.18	2.42	268	797	710	655	554	11	/	/
13-1	0.24	2.60	27.28	0.10	/	247	675	615	585	507	3	/	/
13-2	0.24	2.60	23.79	0.12	/	292	757	690	518	448	5	/	/
13-3	0.24	2.60	21.76	0.13	/	309	797	720	493	420	5	/	/
14	0.09	2.15	23.70	0.04	/	337	701	626	306	246	27	/	/

Note:

[a] No. Experimental number: a total of 21 experiments including five groups of comparative experiments. Each experimental group was labeled with the same prefix number (i.e., 1, 7, 8, 9, and 13). The experiments in each group were performed using the same initial samples but different bulk H_2O density in the HDAC sample chamber, to investigate the effect of pressure on cassiterite crystallization.

[b] $m(SnO_2)$. Initial mass of SnO_2 approximately calculated through the volume of cassiterite crystallized in the sample chamber and cassiterite density (6.95 g/cm^3).

[c] $m(Li_2CO_3)$. Initial mass of Li_2CO_3 approximately calculated through the volume of compacted Li_2CO_3 powder loaded in the sample chamber and the Li_2CO_3 density (2.11 g/cm^3).

[d] $m(H_2O)$. Initial mass of H_2O approximated through the calculated H_2O volume and bulk density determined based on the measured vapor-disappearing temperature and the equation of the state of H_2O (Wagner and Pruβ 2002).

[e] $x(SnO_2)$. Mole fraction of cassiterite crystallized from the aqueous solution calculated through the initial mass of SnO_2, Li_2CO_3, and H_2O in the sample chamber.

[f] $x(Li_2CO_3)$. Mole fraction of Li_2CO_3 in the aqueous solution at T_B calculated through the initial mass of SnO_2, Li_2CO_3, and H_2O in the sample chamber. Note that this calculation method only works for experiments in which no Li_2CO_3 melt droplets appeared in the sample chamber at T_B, ensuring the $x(Li_2CO_3)$ represented the mole fraction of Li_2CO_3 dissolved in aqueous solution at T_B.

[g] T_h. Temperature at which the vapor bubble disappeared in HDAC sample chamber for the vapor bubble generated during cooling process.

[h] T_B. Temperature at which cassiterite crystals began to grow.

[i] T_S. Temperature at which cassiterite crystals stopped growing.

[j] P_B. Approximate pressure at T_B based on the equation of state of H_2O (Wagner and Pruβ 2002) due to the low solubility of Li_2CO_3 in water (Anderson et al. 2001).

[k] P_S. Approximate pressure at T_S.

[l] N. Number of cassiterite crystals formed in the HDAC sample chamber.

[m] v_{aveL}. Average length growth rate of cassiterite for the experiments in which only one main crystal nucleated and grew during cooling.

[n] v_{aveV}. Average volume growth rate of cassiterite for the experiments in which only one main crystal nucleated and grew during cooling.

[o] /. Not determined.

686 Table 2. Experimental results of cassiterite crystallization in the SnO_2–Na_2CO_3–H_2O system.

[a]No.	[b]T_h (°C)	[c]T_B (°C)	[d]T_S (°C)	[e]N	[f]v_{aveL} (10^{-6} cm/s)	[g]v_{aveV} (μm^3/s)
1	354	645	522	1	0.92	3.40
2	220	664	467	27	[h]/	/
3	279	551	390	1	0.73	5.91
4	285	589	397	9	/	/
5	315	584	405	1	0.61	5.43
6	309	476	403	29	/	/
7	269	580	436	15	/	/
8	271	618	459	16	/	/
9	258	659	422	3	/	/
10	245	730	523	4	/	/
11	288	753	619	1	4.92	18.72

687 Note: [a]No., [b]T_h, [c]T_B, [d]T_S, [e]N, [f]v_{aveL}, [g]v_{aveV}, and [h]/ bear the same representations as those described in Table 1.

688

Fig. 1

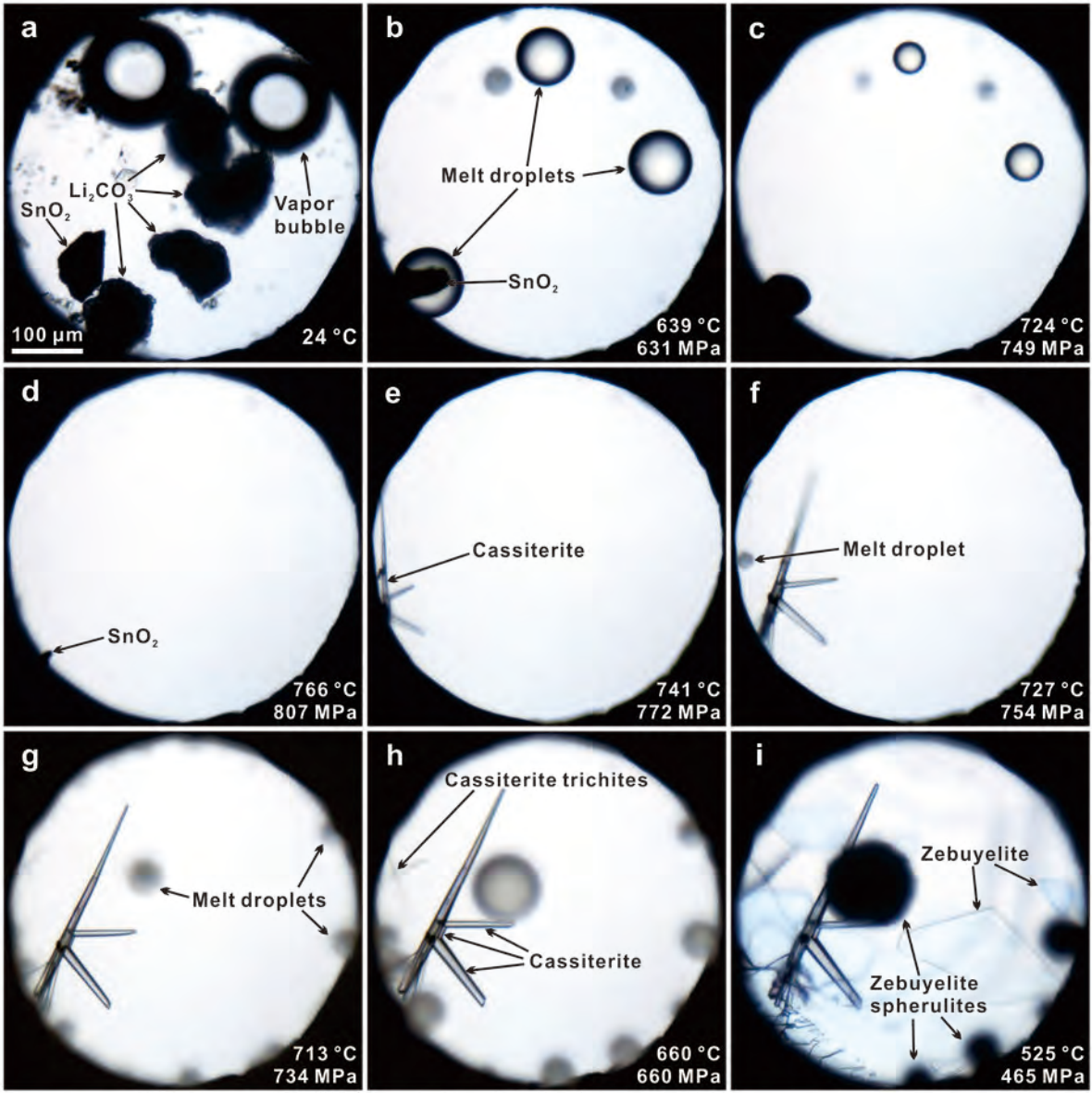
a
Li_2CO_3
SnO_2
Vapor bubble
100 μm
24 °C
b
Melt droplets
SnO_2
639 °C
631 MPa
c
724 °C
749 MPa
d
SnO_2
766 °C
807 MPa
e
Cassiterite
741 °C
772 MPa
f
Melt droplet
727 °C
754 MPa
g
Melt droplets
713 °C
734 MPa
h
Cassiterite trichites
Cassiterite
660 °C
660 MPa
i
Zebuyelite
Zebuyelite spherulites
525 °C
465 MPa

Fig. 2

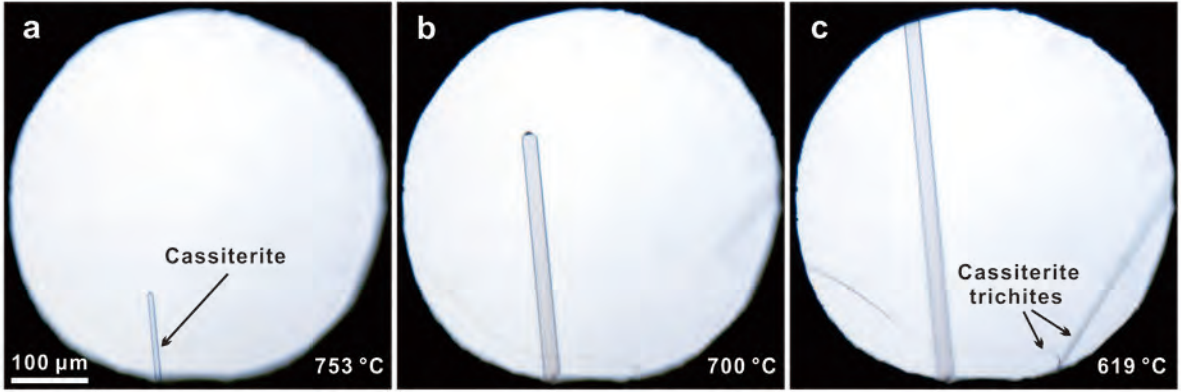
a
Cassiterite
100 µm
753 °C
b
700 °C
c
Cassiterite
trichites
619 °C

Fig. 3

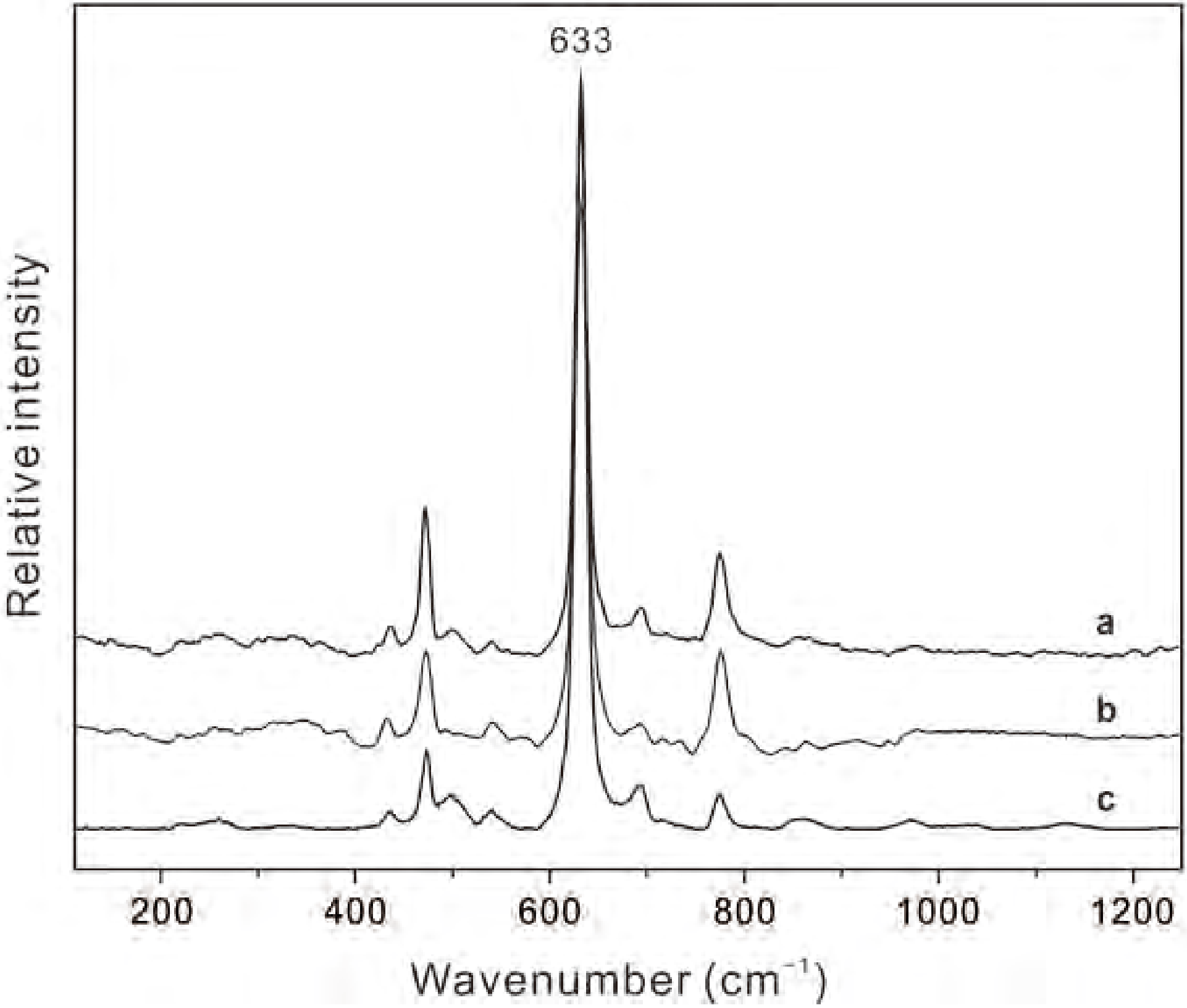
633
Relative intensity
a
b
c
200
400
600
800
1000
1200
Wavenumber (cm^{-1})

Fig. 4

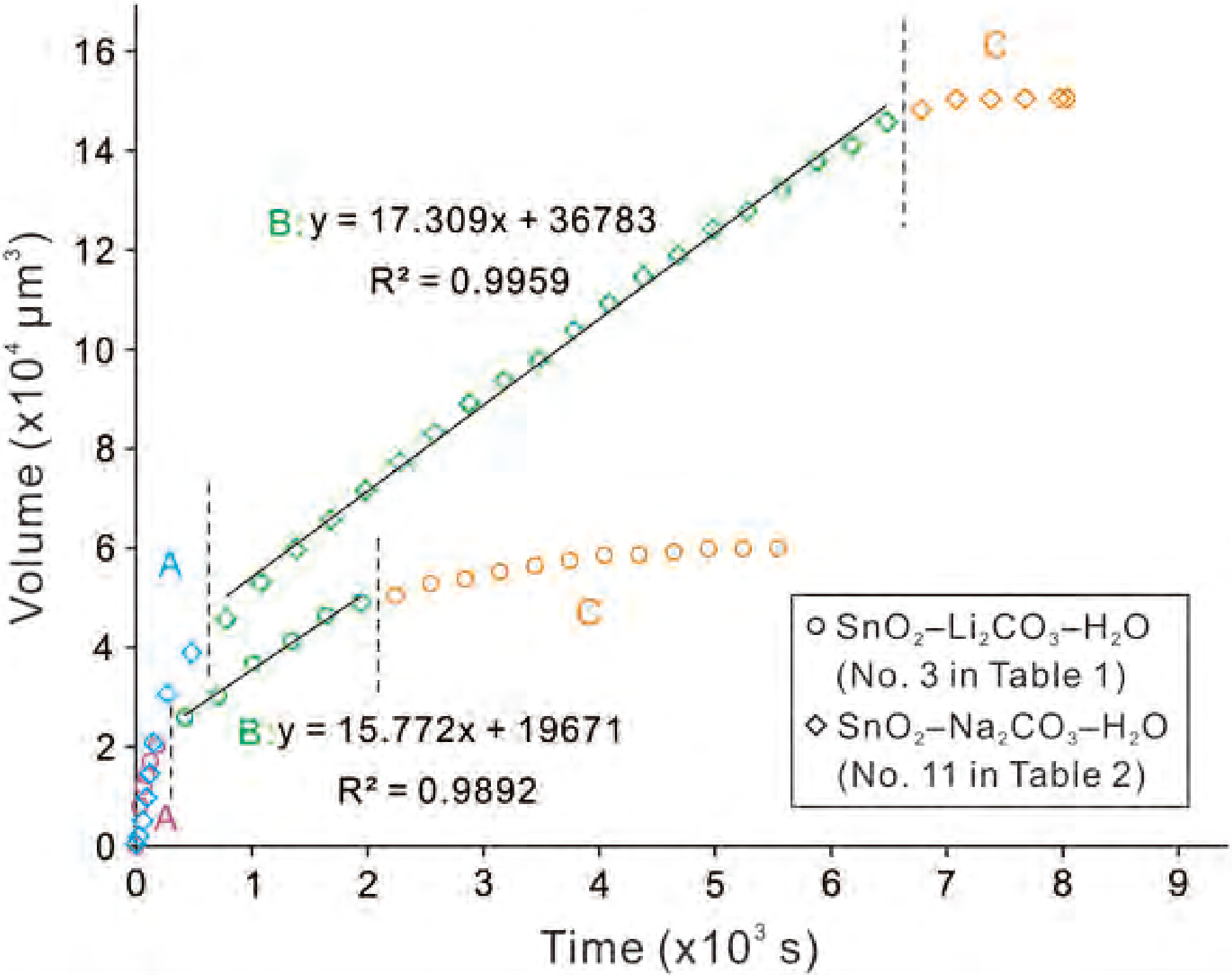
Volume (x10⁴ μm³)
Time (x10³ s)
B: y = 17.309x + 36783
R² = 0.9959
B: y = 15.772x + 19671
R² = 0.9892
A
A
C
C
SnO₂–Li₂CO₃–H₂O
(No. 3 in Table 1)
SnO₂–Na₂CO₃–H₂O
(No. 11 in Table 2)

Fig. 5

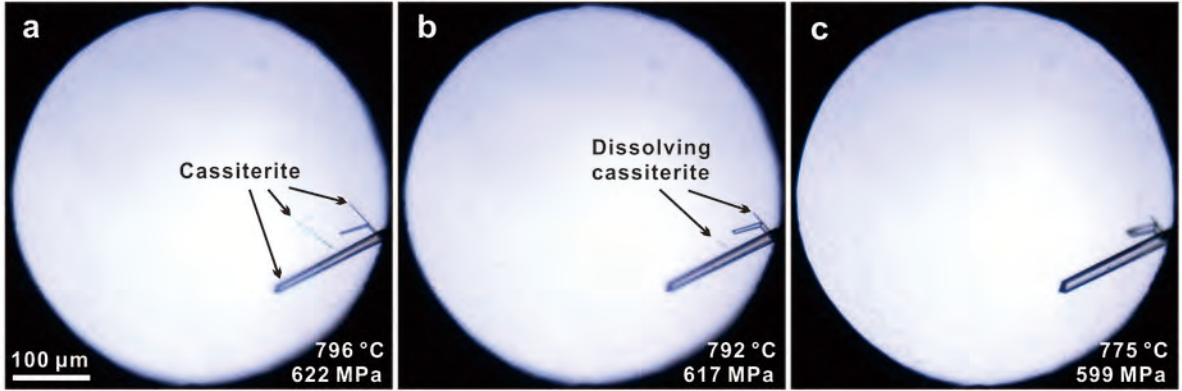
a
Cassiterite
100 µm
796 °C
622 MPa
b
Dissolving
cassiterite
792 °C
617 MPa
c
775 °C
599 MPa

Fig. 6

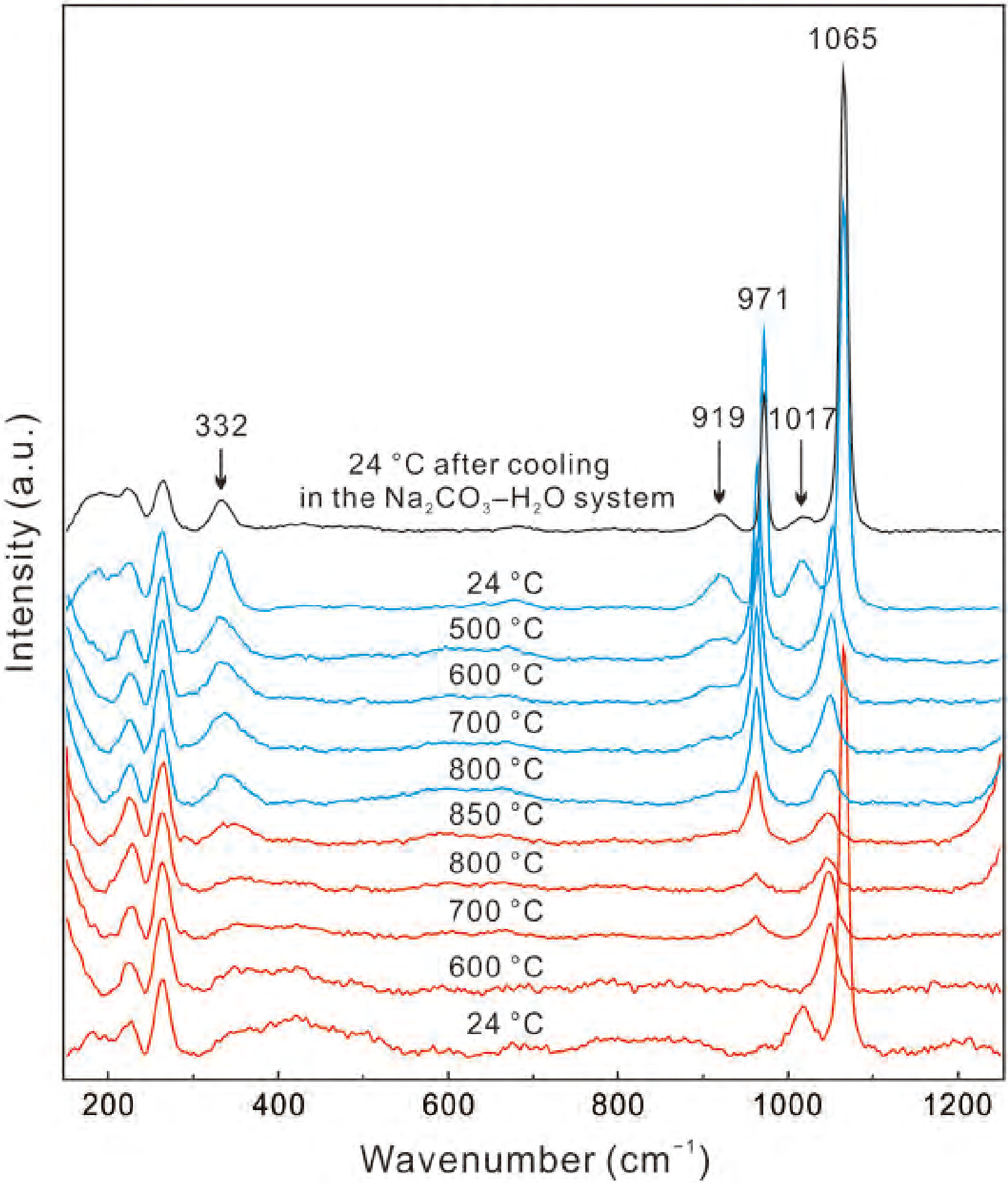
1065
971
919
1017
332
24 °C after cooling
in the Na2CO3–H2O system
24 °C
500 °C
600 °C
700 °C
800 °C
850 °C
800 °C
700 °C
600 °C
24 °C
Intensity (a.u.)
200
400
600
800
1000
1200
Wavenumber (cm−1)

Fig. 7

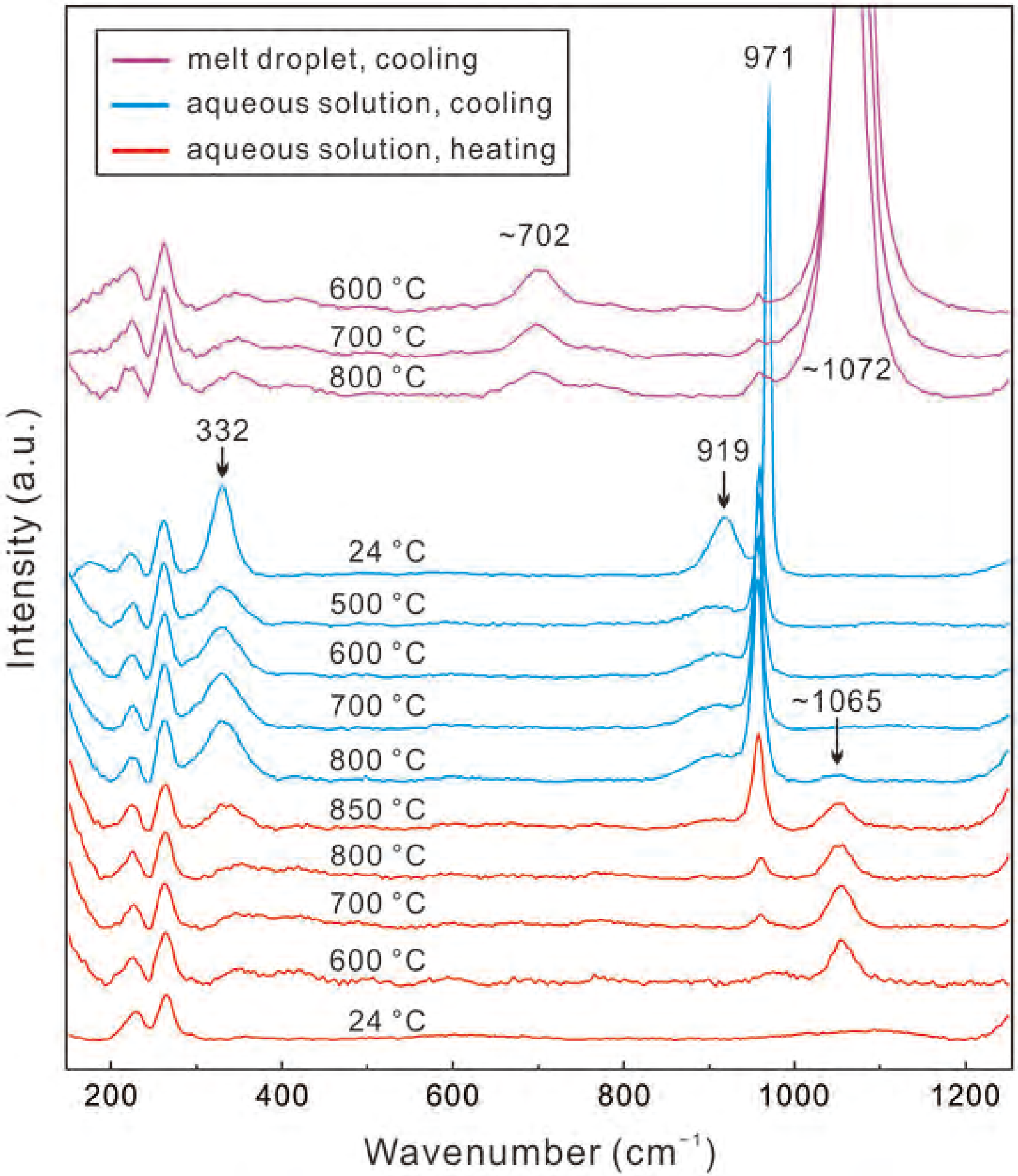
melt droplet, cooling
aqueous solution, cooling
aqueous solution, heating
971
~702
600 °C
700 °C
800 °C
~1072
332
919
24 °C
500 °C
600 °C
700 °C
~1065
800 °C
850 °C
800 °C
700 °C
600 °C
24 °C
Intensity (a.u.)
200
400
600
800
1000
1200
Wavenumber (cm^{-1})

Fig. 8

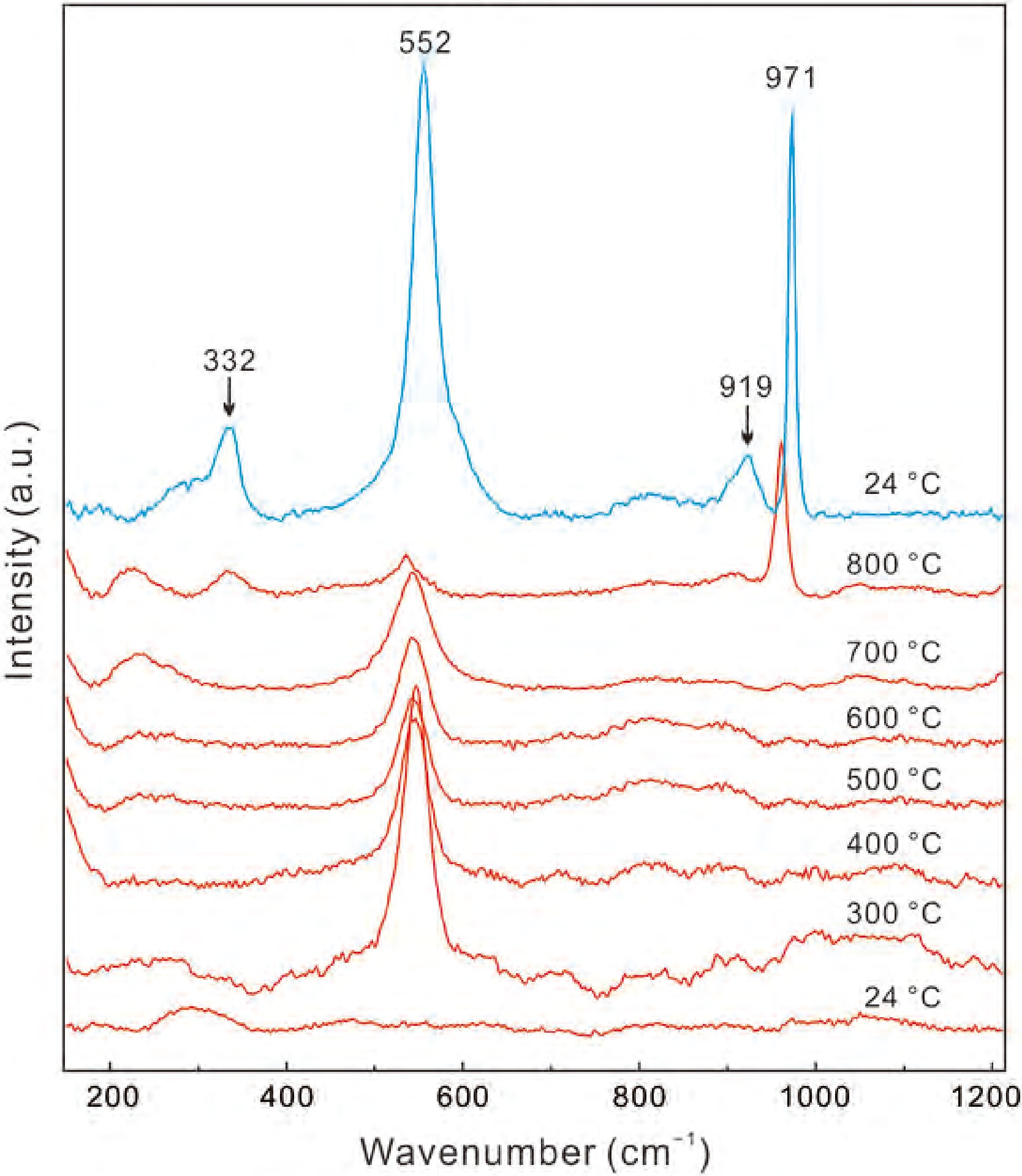
552
971
332
919
24 °C
800 °C
700 °C
600 °C
500 °C
400 °C
300 °C
24 °C
Intensity (a.u.)
200
400
600
800
1000
1200
Wavenumber (cm⁻¹)

Fig. 9

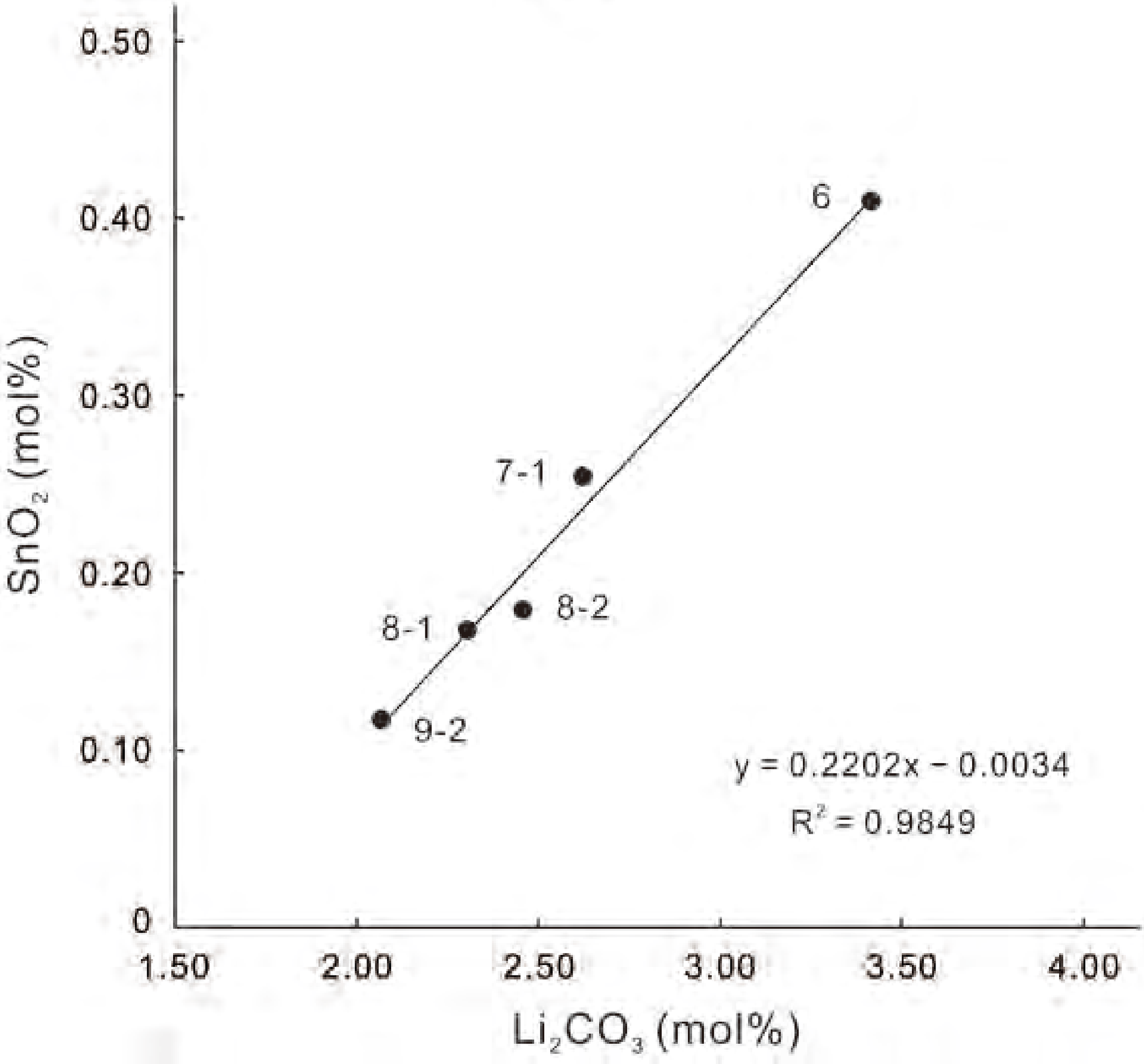
0.50
0.40
0.30
0.20
0.10
0
SnO2 (mol%)
6
7-1
8-2
8-1
9-2
y = 0.2202x − 0.0034
R2 = 0.9849
1.50
2.00
2.50
3.00
3.50
4.00
Li2CO3 (mol%)

Fig. 10

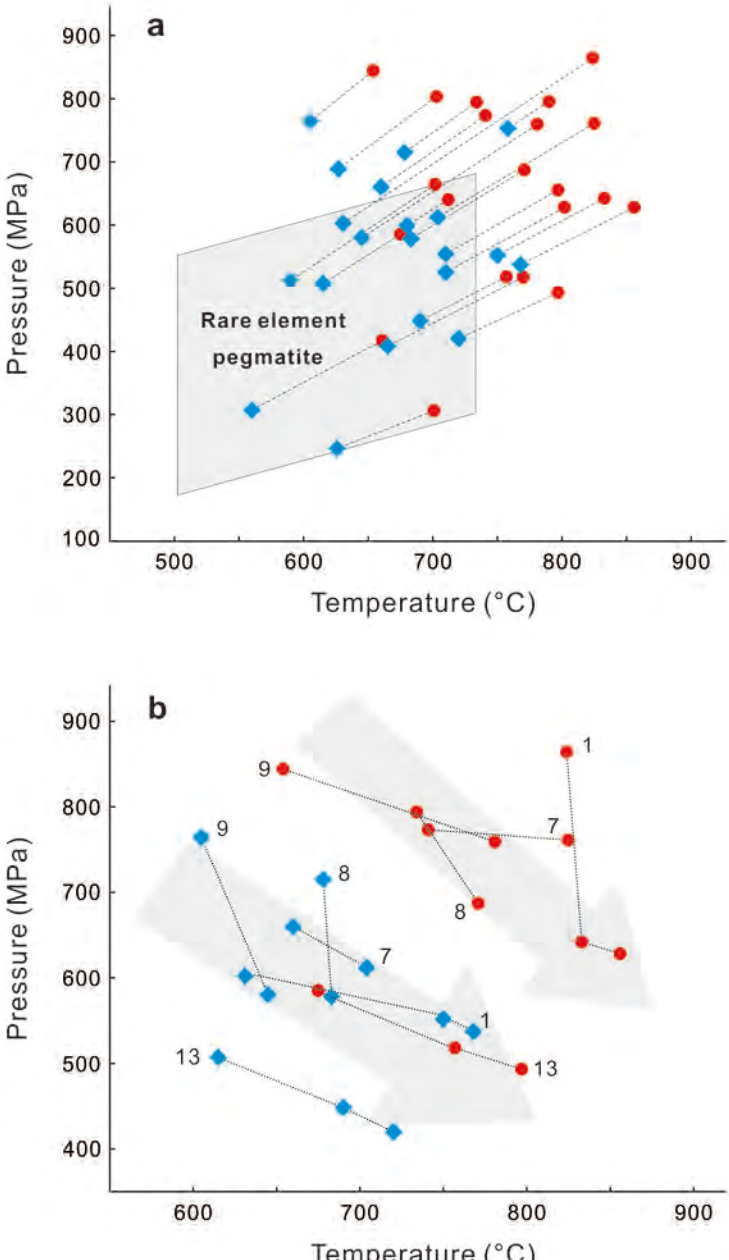
a
Pressure (MPa)
Temperature (°C)
Rare element
pegmatite
b
Pressure (MPa)
Temperature (°C)